Research Square

Preprints are preliminary reports that have not undergone peer review.
They should not be considered conclusive, used to inform clinical practice,
or referenced by the media as validated information.

In Silico Identification of Natural Compound-Derived IL-18 Receptor Alpha Antagonists as Candidate Therapeutics for Graft-versus-Host Disease

Lahoussaine Aserrar

laserrar@um6ss.ma

Mohammed VI University of Sciences and Health (UM6SS), Laboratory of Onco-Pathology, Biology and Cancer Environment, Faculty of Medicine

Hicham Charoute

Research Unit of Epidemiology, Biostatistics and Bioinformatics, Institut Pasteur du Maroc

Salaheddine Redouane

Genomic Sequencing Laboratory, Institut Pasteur du Maroc

Mounia Bendari

Mohammed VI University of Sciences and Health (UM6SS), Laboratory of Onco-Pathology, Biology and Cancer Environment, Faculty of Medicine

Fadila Gessous

Mohammed VI University of Sciences and Health (UM6SS), Laboratory of Onco-Pathology, Biology and Cancer Environment, Faculty of Medicine

---

Article

Keywords: Graft-versus-host disease (GvHD), Interleukin-18 receptor (IL-18R), Molecular docking, Molecular dynamics simulation, Anti-inflammatory, Drug discovery.

Posted Date: May 5th, 2026

DOI: https://doi.org/10.21203/rs.3.rs-9440789/v1

License: This work is licensed under a Creative Commons Attribution 4.0 International License. Read Full License

Additional Declarations: No competing interests reported.

Abstract

Graft-versus-host disease (GvHD) is a life-threatening complication arising after allogeneic hematopoietic stem cell transplantation (allo-HSCT), driven by donor-derived immune cells that recognize and attack host tissues. The interleukin-18 receptor (IL-18R), a member of the IL-1 receptor superfamily, plays a pivotal proinflammatory role in GvHD pathogenesis by mediating IL-18 signaling and promoting IFN-γ production, thereby amplifying the inflammatory cascade underlying disease progression.

In this study, we employed an integrated computational approach that combined molecular docking with AutoDock Vina and molecular dynamics (MD) simulations with GROMACS to identify potential natural inhibitors of IL-18R. A library of bioactive compounds derived from Moroccan medicinal plants with established anti-inflammatory properties, including *Nigella sativa*, *Curcuma longa*, *Rosmarinus officinalis*, and others… was subjected to virtual screening using AutoDock Vina to predict binding modes and affinities. Subsequently, MD simulations were performed to assess the stability of the top-ranked protein–ligand complexes under simulated physiological conditions.

Among the three candidate inhibitors identified (CNP0075206.3, CNP0188167.1, and CNP0196376.4), distinct dynamic behaviors were observed in their interactions with the IL-18Rα chain. Notably, CNP0188167.1 emerged as the most promising candidate, demonstrating the highest binding affinity and the most stable Molecular Dynamics profile, suggesting its potential as a lead inhibitor of IL-18Rα-mediated signaling in GvHD. This computational framework provides a rational and efficient strategy for the pre-experimental screening of natural compounds, thereby accelerating the development of novel therapeutic candidates for GvHD management.

Introduction

IL-18R is a receptor for the interleukin-18 (IL-18), a member of the IL-1 family of cytokines, and plays a proinflammatory role with the ability to induce IFNγ production (Dinarello 1999, 2001). It was initially termed as interferon-gamma-inducing factor (Nakamura et al. 1989). This interleukin binds to the alpha chain of IL18R, and then the IL-18/IL-18Rα complex binds to the Beta chain to form the IL-18/ IL-18Ra/IL-18Rb ternary complex that juxtaposes the intracellular Toll-Interleukin-1 receptor domains of IL-18Rα and IL-18Rβ, enabling the recruitment and the activation of MyD88/NF-κB pathway (Fig. 1) (Tsutsumi et al. 2014; Rex et al. 2020).

IL-18R plays an important role in Graft-versus-host disease (GvHD), a condition that occurs after an allogenic hematopoietic stem cell transplantation, when the immune cells of the donor recognize and attack the recipient's organs, depending on the type of GvHD(Teshima et al. 2016; Zhang et al. 2016; Kanate et al. 2020; Reddy et al. 2020).

Acute GvHD typically occurs within the first 100 days following transplantation and is primarily driven by early alloimmune responses, commonly affecting the skin, liver, and gastrointestinal tract. In contrast, chronic GvHD usually occurs after day 100, and it involves more complex immune dysregulation. It often resembles autoimmune disorders and affects multiple organs, such as the eyes, mouth, lungs, and joints (Pusic and Pavletic 2019; Malard et al. 2023).

Studies show multiple links between the IL-18/IL-18R pathway and GvHD. Increased expression of interleukin-18 receptor on T lymphocytes has been observed in patients with acute graft-versus-host disease after allogeneic bone marrow transplantation (Fujimori et al. 2002). Additionally, upregulation of the interleukin-18 receptor alpha chain was observed in both CD4 + and CD8 + T cells in acute graft-versus-host disease mice (Itoi et al. 2004). Caspase-1-mediated IL-18 release in T cells triggers inflammasome activation, which in turn exacerbates inflammation and increases GvHD severity (Talley et al. 2023). Furthermore, the upregulation of the IL-18R on T cells, caused by IL-

33/ST2, results inincreased IFN-γ production. This further exacerbates GvHD (Reichenbach et al. 2015). Importantly, Neutralizing IL-18Rα with an anti-IL-18Rα monoclonal antibody provides evidence of protective effectsagainst acute graft-versus-host disease in a mouse model (Li et al. 2015).

Current treatments for graft-versus-host disease (GvHD) are mainly based on non-specific immunosuppressors, such as corticosteroids. These treatments, often prescribed empirically, are very toxic and increase the risk of relapse. There is insufficient development of targeted options. Precision medicine requires biomarkers for guidance, such as JAK inhibitors (e.g., ruxolitinib). Although the National Institutes of Health criteria are improving clinical trial design, more effective therapies are still necessary (Pusic and Pavletic 2019).

In our study, we combined molecular docking and molecular dynamics to identify natural inhibitors targeting IL-18R. We conducted molecular docking on bioactive compounds obtained from Moroccan medicinal plants known for their anti-inflammatory activities, including Nigella sativa, Curcuma longa, Rosmarinus officinalis, and others (See Table 1 for the full list). Molecular docking was used to predict the binding mode and binding affinity scores of the candidate ligands (Trott and Olson 2010). In contrast, molecular dynamics simulations were performed to evaluate the stability of the protein-ligand complexes in a simulated physiological environment (Chakravorty et al. 2024).

This computational approach provides a rational method to screen natural compounds before their experimental validation and accelerates the development of novel therapies against GvHD (Fig. 2**)**.

Materials and Methods

Protein structure preparation

The crystal structure of the alpha chain IL-18 receptor was obtained from Protein Data Bank (PDB ID: 3WO3, Resolution: 3.10 Å). Swiss-PDB Viewer was used to model missing regions in the protein structure (Kaplan 2001). Energy minimization of the protein 3D structure was conducted by the steepest descent method using GROMACS. Polar hydrogen atoms and Kollman charges were added using AutoDock Tools (Morris et al. 2009; Goodsell et al. 2021).

Ligands preparation

Natural compounds were extracted from the COCONUT database (3D Structure, SDF Format) for every plant (Sorokina et al. 2021; Chandrasekhar et al. 2025), COCONUT is an open-access database cataloging natural products derived from plants, microorganisms, and marine organisms. It offers structural and biological information for discovering new bioactive molecules. Containing more than 695,000 molecules, COCONUT’s free accessibility and diversity make it ideal for virtual screening(Sorokina et al. 2021; Chandrasekhar et al. 2025).

A total of 3390 sdf molecules with duplicates and 2631 after deleting duplicates. Then the ligands were optimized using the MMFF94 force field and converted to PDBQT format using OpenBabel to proceed with molecular docking.

Active site determination

The identification of active site residues is a key step towards drug design. We used the PrankWeb tool (https://prankweb.cz/) to predict the active site pocket of IL-18R. Also, we conducted a review about the recurrent residues between the active and non-active form of the receptor using PDBsum, and Tsutsumi's study (Tsutsumi et al. 2014) (Table 2).

Molecular docking

Molecular docking was performed using AutoDock Vina v1.1.2. The grid box was positioned over site I, where IL-18 initiates binding to its receptor. Site I in the IL-18Rα receiver corresponds to a large surface area of interaction (~ 1850 Å²) on the surface of the IL-18 tonneau β-trefoil. This region significantly contributes to the first interaction between IL-18 and its primary receptor, IL-18R, and is stabilized by hydrogen and estrogen bonds, including the αlice α1 of IL-18 and other residues like Arg25 of IL-18Rα (Tsutsumi et al. 2014). The selected residues are listed in Table 2. The grid box was centered at coordinates **(x = − 41.953, y = 80.723, z = − 18.154)** with dimensions of **64 × 102 × 80 Å**, encompassing all key site I residues involved in the interaction.

ADMET Properties prediction

Drug-likeness characteristics and ADMET properties (Absorption, Distribution, Metabolism, Excretion, and Toxicity) were identified using ADMETlab 2.0 https://admetmesh.scbdd.com/service/screening/index.

Ligand Screening of Top 10 Candidates and Final Top 3 Selection

We begin by selecting the top 10 ligands with the highest Affinity score from all the docked ligands. Then, we proceed with another top 3 selection for molecular dynamics simulation, starting with the visualization of protein-ligand interactions using Discovery Studio V21.0 software and analyzing the interactions between IL-18R and the Top 10 ligands after docking. The results were displayed as a 2D diagram and saved in the SVG file format. The selection of the three candidate molecules for MD simulation was carried out in two stages. First, analogous molecules or those with a fragmented structure were eliminated to ensure structural diversity (marked “ND”). Next, a weighted score was calculated using the formula: Score = (DockingScore × 0.2) + (MW × 0.5) + (ADMET rules × 0.3), where the DockingScore is rated from 0 to 3 (1 for − 9, 2 for − 10, 3 for ≤ -11 kcal/mol), the molecular weight (MW) is rated from 0 to 3 (0 for > 800 Da, 1 for 701–800 Da, 2 for 621–700 Da, 3 for ≤ 620 Da), and the ADMET rules are 1 if accepted, 0 if rejected (**Supplementary Data)**.

Ligand preparation for MD simulation

Ligand structures in MOL2 format were prepared using OpenBabel to ensure proper hydrogenation and correct ionization state. The SwissParam (https://old.swissparam.ch/) server was used to generate the topology file (.itp) and coordinates file (.pdb), which is compatible with CHARMM. Data from the (.gro) file of the ligands were added to one of the IL-18R, and then the (.itp) file was incorporated into the topol.top file, all these parameters were performed to ensure the compatibility of the complex with GROMACS algorithms before minimisation and equilibration (Supplementary data).

Molecular dynamics simulation

Molecular dynamics (MD) simulations were carried out using GROMACS v.2021 with the CHARMM force field. The systems were solvated in a TIP3P water box with a 10 Å margin and neutralized by adding Na^+ and Cl^- ions. Energy minimization was performed using the conjugate gradient algorithm over 50,000 steps. Equilibration was then conducted under NVT conditions (100 ps at 310 K), followed by NPT conditions (100 ps at 1 bar). A 340 ns production run was performed using a 2 fs time step, with trajectory snapshots saved every 10 ps (Script supplementary data).

Trajectory analysis allowed us to evaluate the stability of the systems. Root Mean Square Deviation (RMSD) was calculated to assess the global conformational evolution of the backbone. Root Mean Square Fluctuation (RMSF) was used to identify the flexibility of the protein. The radius of gyration (RG) provides information about the compactness of the protein structure. Hydrogen bonds (H-BONDS) help elucidate the number of hydrogen bonds created between the ligand and the protein during the simulation. Solvent-Accessible Surface Area (SASA) was analyzed to evaluate changes in residue accessibility by the solvent. Potential energy (PE) is the total sum of all specific energetic terms of the simulation.

Principal Component Analysis and Free Energy Landscape

Principal Component Analysis (PCA) was performed to identify the major collective motions of the protein conformations. Finally, the Free Energy Landscape (FEL) allows for visualizing and identifying energy wells corresponding to the conformations favored (All Gromacs commands are described in the Scripts Supplementary data).

Supplementary analyses extracted using Python

Supplementary analyses were performed using Python scripts, starting with **RMSD boxplots** of the ligands and the protein using the Wilcoxon test, which allowed us to compare the distribution of the mean deviations between the complexes and between the ligands, indicating the variability and the global stability of the complexes and the ligands. The plot of the PE vs RMSD was used to visualize the correlation between the conformational stability and the energetic stability. This allows us to identify the most favorable stats. Moreover, the Time Colored PCA serves to examine the temporal evolution of the conformation clusters explored in each complex.

Table 1
Selected plants for Molecular Docking

Plantes	***Study***	***Plantes***	***Study***
Ammi visnaga	Abdelhakim Bouyahy al. (2022)	Mentha pulegium	Firouz Mohammadi et al. (2024)
Ammodaucus leucotrichus	Abdelhakim Bouyahy al. (2022)	Nasturtium officinale	Klimek-Szczykutowicz et al. (2018)
Anacyclus pyrethrum	Elazzouzi et al. (2022)	Nigella sativa	Bourgou et al. (2010)
Argania spinosa	Abdelhakim Bouyahy al. (2022)	Olea europaea	El & Karakaya (2009)
Argania spinosa	Rachida Makbal et al. (2021)	Opuntia ficus-indica	Wen-Chien Lu (2023)
Artemisia herba-alba	Daycem Khlifi et al. (2013)	Origanum vulgare	Rosanna Avola et al. (2020)
Asphodelus microcarpus	Abdelhakim Bouyahy al. (2022)	Papaver rhoeas	Abdelhakim Bouyahy al. (2022)
Berberis vulgaris	Abdelhakim Bouyahy al. (2022)	Pelargonium graveolens	Abdelhakim Bouyahy al. (2022)
Calendula arvensis	Abdelhakim Bouyahy al. (2022)	Pistacia lentiscus	Chabha Sehaki et al. (2023)
Capparis spinosa	Khadija El Azhary et al. (2017)	Retama monosperma	El Yadini et al. (2023)
Centaurium erythraea	El Menyiy et al. (2021)	Retama raetam	Abdelhakim Bouyahy al. (2022)
Ceratonia siliqua	Abdelhakim Bouyahy al. (2022)	Rosmarinus officinalis	Raphaelle Sousa Borges et al. (2018)
Ceratonia siliqua	Attia H Atta et al. (2023)	Sideritis arborescens	Abdelhakim Bouyahy al. (2022)
Chamaerops humilis	Abdelhakim Bouyahy al. (2022)	Syzygium aromaticum	Abdelhakim Bouyahy al. (2022)
Cistus monspeliensis	Abdelhakim Bouyahy al. (2022)	Tetraclinis articulata	Abdelhakim Bouyahy al. (2022)
Cistus salviifolius	Abdelhakim Bouyahy al. (2022)	Thymus Algeriensis	Mansour Sobeh et al. (2020)
Citrus aurantium L	Abdelhakim Bouyahy al. (2022)	Thymus hirtus	Lahlou et al. (2022)
Citrus limon	Abdelhakim Bouyahy al. (2022)	Thymus vulgaris	Abdelhakim Bouyahy al. (2022)
Cupressus sempervirens	Abdelhakim Bouyahy al. (2022)	Thymus vulgaris	Farah M Abdelhamed et al. (2022)
Curcuma longa	Aggarwal & Harikumar (2009)	Viscum album	Abdelhakim Bouyahy al. (2022)
Equisetum arvense	Abdelhakim Bouyahy al. (2022)	Withania frutescens	Bouissane et al. (2024)
Eucalyptus globulus	Abdelhakim Bouyahy al. (2022)	Zingiber officinale	Fitriyono Ayustaningwarno al. (2024)

Plantes	*Study*	*Plantes*	*Study*
Foeniculum vulgare	Abdelhakim Bouyahy al. (2022)	Ziziphus lotus	Abdelhakim Bouyahy al. (2022)
Genista tridentata	Laranjeira et al. (2023)	Zygophyllum gaetulum	Abdelhakim Bouyahy al. (2022)
Haloxylon scoparium	Abdelhakim Bouyahy al. (2022)	Marrubium vulgare	Abdelhakim Bouyahy al. (2022)
Jasonia glutinosa	Valero et al. (2025)	Melissa officinalis	Abdelhakim Bouyahy al. (2022)
Lavandula stoechas	Francesca Algieri et al. (2016)	**Flueggea virosa**	Diarra et al. (2024)

Table 2
Determined IL-18Rα Active Site Residues

Recurrent residues according to PDBsum profiles of 3WO3 and 3WO4 for IL-18Rα	**According to the topological pocket predictions using (PrankWeb)**	**According to Tsutsumi et al. 2014 (Site I)**
Cys22	Tyr23	Ser127
Tyr23	Arg25	Gln124
Ser24	Iso28	Arg25
Arg25	Thr29	His27
Pro26	Val30	Cys22
His27	Glu34	Cys41
Iso28	Pro35	Cys43
Thr29	Phe36	Cys81
Cys43	Tyr37	Ser24
Arg123	Glu141	Lys128
Glu124	Asp142	Ser42
Val125	Tyr144	
Tyr126	Tyr145	
Ser127	Iso198	

Results

Docking Results

We select a total of 2631 ligands extracted from Moroccan plants that were evaluated by molecular docking against the interleukin-18 receptor alpha chain (IL-18Rα). representing the natural compounds identified in the selected medicinal plants. After removing redundant molecules, 2,631 unique structures were retained and converted to PDBQT (Protein Data Bank, Partial Charge and Atom Type) format, which is required for molecular docking with AutoDock Vina. Of the 2,631 molecules prepared, 2,612 were successfully docked to the protein target. The slight difference (19 molecules) is due to conversion failures or structural incompatibilities during docking.

The docking results are distributed according to free binding energy (ΔG in kcal/mol): 2 molecules with ΔG ≤ -11 kcal/mol (excellent affinity), 6 molecules with ΔG = -10 kcal/mol (very good affinity), 37 molecules with ΔG = -9 kcal/mol (good affinity), 292 molecules with ΔG = -8 kcal/mol (moderate affinity), 2,275 molecules with scores greater than − 8 kcal/mol (low affinity) (Fig. 3.a).

Top 10 highest affinity score Ligands were selected to be evaluated in Drug-likeness characteristics and ADMET properties with ADMETlab 2.0, and Structure state with Discovery studio, CNP0238863.1 and CNP0238863.4 were eliminated for their fragmented structure, CNP0115399.1 CNP0232905.2 and CNP0232905.1 were eliminated due to the big analogy structurally and chemically with CNP0188167.1 that is selected only due to his highest affinity score, Then the rest of the ligands were CNP0188167.1 CNP0075206.3 and CNP0196376.4 were chosen from the rest as Top 3 ligands selected for MD simulation based on a score of selection (Table 3).

b) Chemical structures and plant sources of selected natural compounds and their structural analogs. Among the 10 molecules with the highest binding affinities, three were selected for molecular dynamics simulation after elimination of fragmented structures (red), redundant analogues (blue), and compounds with low Selection scores (yellow). The three molecules selected (green) come from different Moroccan medicinal plants: **CNP0188167.1**, a securinane-type alkaloid (analog of Norsecurinine/Fluevirosinine) isolated from Flueggea virosa; **CNP0075206.3**, an anthraquinone dimer known as Asphodeline from Asphodelus microcarpus; and **CNP0196376.4**, a flavonoid derived from quercetin extracted from Cupressus sempervirens.

Table 3
Top 10 Candidates and Final Top 3 Selection

Ligand ID	DockingScore	MW	Lipinski	Pfizer	GSK	GoldenTriangle	Selection Score (Top 3)
CNP0238863.1	-10.10	660.23	Rejected	Accepted	Rejected	Rejected	ND
CNP0238863.4	-10.10	660.23	Rejected	Accepted	Rejected	Rejected	ND
CNP0115399.1	-10.00	609.28	Accepted	Accepted	Rejected	Rejected	ND
CNP0232905.2	-10.90	623.3	Accepted	Accepted	Rejected	Rejected	ND
CNP0232905.1	-10.60	623.3	Accepted	Accepted	Rejected	Rejected	ND
CNP0188167.1	-11.50	609.28	Accepted	Accepted	Rejected	Rejected	2,7
CNP0075206.3	-10.00	640.16	Rejected	Accepted	Rejected	Rejected	1,7
CNP0196376.4	-9.80	756.21	Rejected	Accepted	Rejected	Rejected	1
CNP0253739.1	-11.80	818.43	Rejected	Accepted	Rejected	Rejected	0,9
CNP0076333.1	-9.80	1106.11	Rejected	Accepted	Rejected	Rejected	0,5
ND: Not Determined							

Discovery Studio Analysis:

Among the three top-scoring ligands, **CNP0188167.1** showed the **best binding affinity**. It forms a **conventional hydrogen bond** with **THR29** residue and a **carbon-hydrogen** bond with **GLN129** residue, and a **hydrophobic alkyl** interaction with **Lys200**. However, its overall interaction network in DS appears sparse compared to the other ligands, with fewer anchoring points inside the binding pocket. The second ligand, **CNP0075206.3**, presents a more complex interaction profile, involving conventional **hydrogen bonds** with **THR29**, **ARG25, THR199, and HIS27**, as well as **π–**

cation interaction with **ARG25** and **π–alkyl** interaction with **LYS200** and **π–π T-shaped** with **PHE36**. The third ligand, **CNP0196376.4**, forms multiple hydrogen bonds with **GLU141, ASN142, SER143**, and **ARG25**, along with **carbon-hydrogen** bonds and **hydrophobic alkyl** interaction with **Lys200**, and unfavorable donor-donor interactions with **SER24** and **THR29** (Fig. 4).

Drug Likeness Analysis:

ADMETlab 2.0 analysis provides comprehensive **ADMET** profiling and structural validation for the docked compounds. All three ligands show rejection in multiple drug-like property filters, indicating potential challenges for oral bioavailability and pharmaceutical development. **CNP0188167.1** has a complex **tetracyclic** structure with several **oxa-aza** bridge systems, which probably contribute to its exceptional complementarity with the receptor. With a molecular mass of **609.28 Da**, the compound remains within acceptable limits, although its drug-like properties are mixed. Its complex polycyclic architecture, although offering high binding affinity, could pose synthesis challenges and potential metabolic instability. However, its acceptance by some filters suggests that it retains favorable properties despite its structural complexity, **CNP0075206.3**, with a binding score of -10.00 kcal/mol, exhibits an anthracene-derived structure comprising multiple hydroxyl groups and a **trihydroxytetrahydropyran** motif, suggesting an extensive hydrogen bond network with the receptor. With a molecular mass of **640.16 Da**, this compound only partially meets the drug-likeness criteria. Its polyhydroxy anthracene core indicates a potential for strong interactions with the receptor, but also raises concerns about its solubility and elimination mechanisms. **CNP0196376.4**, with a binding score of -9.80 kcal/mol, is a glycosylated flavonoid derivative with the highest molecular mass (**756.21 Da**). Its structure includes several sweet units, which could improve its selectivity but also compromise its membrane permeability. Its **glycosidic** nature, evident from its flavonoid-sugar conjugated structure, suggests that it may require transporter-dependent absorption and be subject to rapid hepatic metabolism (Table 3).

MOE Analysis:

CNP0196376.4 This ligand represents a complex structure with several fused aromatic rings and multiple hydroxyl (-OH) groups. The molecule exhibits an excellent complementarity with the binding site, establishing numerous hydrogen bonds through its polar groups. The interactions extend over a large surface area of the receptor, with preferred contacts with polar and basic residues. The adopted conformation allows for deep anchoring in the binding pocket, suggesting high affinity. The blue contours, representing the proximity zones, indicate an optimal adaptation to the topology of the active site. **CNP0188167.1** This molecule represents a more compact architecture based on ring systems fused with heteroatoms. The structure gives it a defined geometry that specifically inserts into a particular region of the IL-18R receptor. Although exhibiting fewer hydrogen bonds than the first compound, it establishes selective contacts with key residues in the binding site. The distribution of interactions suggests a different, potentially allosteric, binding mode, with a preference for hydrophobic and π-π interactions with aromatic residues. **CNP0075206.3** This ligand is characterized by an extended and flexible structure combining several structural motifs: aromatic rings, aliphatic chains, and polar functional groups. Its elongated conformation allows it to interact with multiple receptor subsites simultaneously. The multiple hydroxyl groups and aromatic systems create a diverse network of interactions, including hydrogen bonds, π-π interactions, and hydrophobic contacts. This spatial distribution of interactions suggests a versatile binding capacity with IL-18R, capable of modulating different aspects of receptor function (Fig. 5).

Molecular Dynamics Results:

Protein Root Mean Square Deviations:

CNP0075206.3 and **CNP0188167.1** induce similar Protein RMSD (~ 1.85–1.90 nm) in the boxplots, and fluctuations between (~ 1,20-2.25 nm) in the trajectory curves, suggesting a stable conformation of the receptor with the 2 ligands. **CNP0196376.4** triggers a highly significant Protein RMSD (~ 2.35 nm), indicating a structural perturbation more pronounced for the receptor, especially between 50 ns and 100 ns, which increases from approximately 1.5 to 2.25 nm. Still, from 210 ns we can notice a high stability that continues until the end. The difference is statistically significant ($p < 0.001$), with the **CNP0196376.4** inducing around 20–25% of the structural deviations more than the other 2 ligands **(**Fig. 6.**a/6.c)**.

Ligans Root Mean Square Deviations

CNP0188167.1 represents the lowest RMSD (~ 0.04 nm), indicating a high stability in the active site. **CNP0075206.3** shows an intermediate RMSD (~ 0.12 nm), suggesting a moderate stability. **CNP0196376.4** shows a high RMSD (~ 0.35 nm), reveals an important and considerable mobility and flexibility. The Wilcoxon test confirms that these differences are highly significant ($p < 0.001$ for all comparisons), demonstrating distinct behaviors for each ligand. Temporal evolution shows that **CNP0196376.4** maintains its high flexibility along the simulation, while **CNP0188167.1** stays remarkably stable, and **CNP0075206.3** represents moderate fluctuations with a few occasional pics **(**Fig. 6.**b/6.d)**.

Potential energy

CNP0188167.1 et **CNP007** present a potential energy very similar (~-2.490 to -2.495 kJ/mol), indicating an equal and stable energetic system. **CNP0196376.4** shows less favorable potential energy (~-2.475 kJ/mol), which is approximately 15–20 kJ/mol higher. These significant energetic differences suggest that **CNP0196376.4** forms less optimal interactions with the receptor **(**Fig. 6.**h).**

Hydrogen Bonds

CNP0196376.4 Forms the highest number of H bonds (fluctuating between 2–9, with 5–8 bonds frequent pics), **CNP007** maintains a moderate number of H bonds (Generally 0–4). **CNP0188167.1** presents fewer H bonds (Generally 0–2) with few pics **(**Fig. 6.**i)**.

Radius of Gyration

CNP007 and **CNP0188167.1** rapidly reach a stable equilibrium (~ 2.25–2.35 nm) within the first 50 ns. In contrast, CNP0196376.4 exhibits a prolonged adaptation phase, characterized by an initially high Rg (~ 3.0-3.4 nm) from 0 to 100 ns. Then it decreases progressively to converge into ~ 2.30 nm after 200 ns **(**Fig. 6.**f)**.

Root Mean Square Fluctuations

The three ligands show a major common pic with maximal fluctuations around residue 60, suggesting a flexible region in the receptor. **CNP0196376.4** induces the most important fluctuations in a lot of regions (residues 200–220, 270–320). **CNP0188167.1** generates the least fluctuations and is homogeneous along the sequence. **CNP0075206.3** represents the intermediate profile of fluctuations **(**Fig. 6.**e)**.

Flexibility analysis identified several key regions in all three profiles. The N-terminal region (residues 1–25) exhibits high initial flexibility. An area of high flexibility, probably a functional loop, is observed between residues 40 and 60. A second sensitive region, linked to the ligand, is located at residues 200–220. Finally, residues 270–330 show significant fluctuations, particularly in the presence of the **CNP0196376.4** and **CNP0188167.1** ligand **(**Fig. 6.**e)**.

Correlation protein RMSD vs Potential energy

The plot reveals crucial information about the relation between the structural deformation and the energetic stability of the complexes. **CNP0188167.1** represents an optimal compact cluster, forms a dense cluster, and is well defined in the low-energy regions (-2.490 à -2.500 kJ/mol). Also, the Protein RMSD concentrates between 1.5 and 2.5 nm. **CNP0075206.3** represents a similar cluster to **CNP0188167.1**, with a minor accrued dispersion. Potential energy is in the same favorable range (-2.485 à -2.495 kJ/mol), and also the RMSD is similar, 1.5–2.5 nm. **CNP0196376.4** represents an unfavorable energetic dispersion and Distribution, characterized by larger and more dispersed particles. The potential energy is systematically higher (-2.465 à -2.480 kJ/mol), RMSD is too wide (0.5–2.5 nm), including the initial rearrangement phase **(**Fig. 6.**g)**.

Solvent accessible surface areas

SASA measures the exposition of the complex protein-ligand to the aqueous solvent, reflecting the conformational changes and the compactness of the system. **CNP0196376.4** represents a SASA initially high (~ 245–260 nm²) during the first 100 ns, then we observed a progressive diminution around ~ 195–210 nm² between 100 and 200 ns. The SASA is clearly low in the final phase. **CNP0075206.3 and CNP0188167.1** begin with a high SASA (~ 220–245 nm²), but with a fast stabilization, **CNP0075206.3** stabilizes around ~ 200–230 nm² after 50 ns, with a small decrease from ~ 190 nm² to 170 ns, **CNP0188167.1** stabilizes around ~ 200–230 nm² after 50 ns, with an equilibration faster than CNP019. **CNP0075206.3** presents moderate fluctuations; a stable profile reflects a normal "respiration" of the protein. **CNP0188167.1** presents a quasi-identical profile with **CNP0075206.3 (**Fig. 6.**j)**.

Principal Component Analysis

PCA reveals the distribution of the conformational states explored by each complex (protein-ligand) during the simulation. The first two (PC1 and PC2) capture the dominant movements of the system. Comparing the 3 complexes. The global visualization reveals a remarkable horseshoe effect in the three profiles and differences in the conformational exploration. **CNP0196376.4** with an extensive conformational Exploration holds the most volume of the space of PC1-PC2, and an extensive distribution: PC1 [-40 to + 120], PC2 [-45 to + 50], forming a lot of distinct clusters, suggesting multiple conformational states. **CNP0075206.3** with an intermediate Exploration, comes with a moderate distribution: PC1 [-30 to + 60], PC2 [-30 to + 30], forms a relatively compact cluster with few excursions. **CNP0188167.1** with an optimal conformational Confinement, comes with the most restricted distribution: PC1 [-60 to + 50], PC2 [-25 to + 40], compact Cluster and well defined, occupying distinct regions of the conformational space **(**Fig. 7.**a)**.

Separated PCA clusters with temporal evolution in the space

Separating the 3 complexes and adding temporal evolution shows how each ligand induces distinct movements in the IL-18Rα, and as we examine the temporal evolution of the clusters along the simulation. **CNP0188167.1** starts with an initial phase (0–50 ns, deep violet to blue), positioned in PC1 [-60 to -40], PC2 [+ 10 to + 40], characterized by a compact Cluster from the beginning, and a fast Transition into a new state. Then a transition continues phase (50–200 ns, blue → cyan → green), positioned in PC1 [-40 to + 20], PC2 [+ 40 to -20], with remarkable fluid quasi-circular movements along the trajectory. Space rotation in the PC (anti-clockwise) with a gradual and organized evolution and no sudden jumps. And ends with the equilibrium Phase (200–340 ns, light green to yellow), Last Stabilisations: PC1 [+ 20 to + 40], PC2 [-20 to + 30], with extremely compact and dense clusters, especially at the end. Characterized by the tightest distribution among the three complexes **(**Fig. 7.**a)**. **CNP0075206.3** starts with an initial Phase (0–50 ns, violet to deep blue), Stabilising in the region PC1 [+ 20 to + 60], PC2 [+ 10 to -30], with a dense cluster indicating a convergence to a stable state, and a few minor excursions reflecting normal thermic fluctuations. Transition phase (50–150 ns, bleu → cyan → green) reveals a Migration into PC1 [-10 to + 20], PC2 [+ 10 to + 30], characterized by a systematic Exploration of a new conformational basin, coordinated Movement suggesting an oriented structural

relaxation. Equilibrium Phase (150–340 ns, Light green to yellow), with the Position: PC1 [-40 to -10], PC2 [-20 to + 10], the system starts from an initial state and explores the conformational space. Also, we remark a visible gradual transition and a large conformational dispersion **(**Fig. 7.**b)**. **CNP0196376.4**, with a unique profile, starts with an initial/exploration phase (50–150 ns, deep violet to blue), remarekabl Dispersion in PC1 [+ 60 to + 120], PC2 [-45 to + 20] characterized by no convergence, especially after 130 ns, Formation of multiples secondary clusters followed by a progressive Migration to PC1 [+ 40 to + 80], PC2 [-40 to + 20] characterized by Maintained importante Dispersion with several trajectory visible branches, and the formation of two sub-clusters. The system hesitates between many conformational states. Phase of majeure transition (150–250 ns, blue to cyan), less large distribution: PC1 [-10 to + 40], PC2 [+ 20 to + 50], remarkable convergence into a stable state. Tardive Phase (250–340 ns, cyan → green → yellow), starting by the position PC1 [-20 to 0], PC2 [20 to 0], and fast transition to PC1 [-40 to -20], PC2 [0 to -25], ample movement and fast characterized by dense and stable clusters in the end. **(**Fig. 7.**c)**.

Free Energy landscape

The FEL of **CNP0188167.1** presents an exceptional energy landscape dominated by a single deep basin centered at PC1 between ~ 0 and 2.5, PC2 between ~ 6 and 8, with a minimum free energy between 0 and 2.5 kJ/mol. This basin captures more than 85–90% of the total population, forming a funnel-shaped topography characteristic of high-affinity complexes. The marginal peripheral basins at PC1 between ~ 5 and 10, PC2 between ~-7 and 7, are separated by barriers greater than 10 kJ/mol, making these states virtually inaccessible. **CNP0196376.4** - Frustrated and diffuse landscape with no dominant minimum **(**Fig. 7.**a)**. **CNP0075206.3** reveals a complex energy landscape characterized by two distinct main basins. The most favorable basin is located at PC1 between ~-7.5 and − 5, PC2 between ~ 0 and ~ 3, with a minimum free energy of 2.5 kJ/mol, and the second is located at PC1 between ~-9.5 and − 7, PC2 between ~ 3 and ~ 5.5, with a minimum free energy of 2.5 kJ/mol, representing approximately 35–40% of the total population. With the two recent basins, we also note the presence of five other basins with a minimum free energy of 5 kJ/mol, three located at PC1 between − 5 and 1, PC2 between − 5 and − 9.5, and two others at PC1 between 5 and 10, PC2 between 0 and 9 **(**Fig. 7.**b)**. The FEL of **CNP0196376.4** shows a particularly unfavorable energy landscape, characterized by five to six shallow basins with no clearly defined global minimum. Free energies range from 5 to 15 kJ/mol, with the most populated basin (PC1 between ~-7.5 and − 10, PC2 between ~ 1.5 and ~-5) reaching only 30–35% of the population at an energy between 0 and 2.5 kJ/mol. The vast dominant cyan-green area indicates a diffuse energy distribution with multiple conformations of similar energy, typical of fundamental energy frustration **(**Fig. 7.**c)**.

Discussion

The three ligands studied (CNP0196376.4, CNP0188167.1, and CNP0075206.3) are semi-synthetic derivatives of natural molecules. CNP0188167.1 is derived from quercetin, an anti-inflammatory flavonoid from Flueggea virosa, extracts of which have been shown to inhibit pro-inflammatory cytokines (Diarra et al. 2024). CNP0075206.3 comes from Asphodelus microcarpus, a Mediterranean plant whose anthraquinone derivatives modulate inflammatory signaling pathways (Bouyahya et al. 2022). CNP0196376.4 is an asphodeline analog derived from Cupressus sempervirens, with documented anti-inflammatory properties (Khalfaoui et al. 2021; Bouyahya et al. 2022).

CNP0188167.1: primary competitive inhibitor. With an anchor score of -11.50 kcal/mol, this ligand has the highest affinity for IL-18Rα. Despite a high molecular weight (609.28 g/mol) that makes it non-compliant with Lipinski's rule, its acceptance by Pfizer criteria positions it as an injectable candidate (Walters 2012). It forms hydrogen bonds with THR29 (active site) and GLN129, as well as a carbon-hydrogen bond with LYS200, interactions that collectively explain its exceptional score (Morris et al. 2009; Adasme et al. 2021).

MD simulation (GROMACS) confirms this stability: lowest RMSD, optimal potential energy, stable radius of gyration (2.25–2.35 nm), and low RMSF fluctuations. PCA reveals optimal conformational confinement with organized temporal evolution. The FEL has a deep, single well (0–2.5 kJ/mol), characteristic of high-affinity complexes, predicting favorable kinetics (high kon, low koff) (Bernetti et al. 2017). Its injectable administration is viable, particularly in a post-transplant setting (Xu et al. 2011; Nakmode et al. 2025).

CNP0075206.3 is considered a modulator to be optimized. With an anchor score of -10.00 kcal/mol, this ligand interacts with 4 residues of the active site (PHE36, ARG25, HIS27, THR29) via π-π interactions in T with PHE36 and π-cation interactions with ARG25, suggesting a potential disruption of receptor dimerization (Gohlke and Klebe 2002). However, its high molecular weight (640.16 g/mol) poses pharmacokinetic challenges.

In MD simulation, its intermediate behavior is consistent with this moderate affinity: moderate RMSD, occasional conformational fluctuations, and variable hydrogen bonds (0–4). The bifurcated FEL with two main basins (~ 2.5 kJ/mol) and five secondary basins (~ 5 kJ/mol) indicates multiple binding modes and some flexibility (Qiang et al. 2025). Its optimization should aim either to stabilize the favorable basin by strengthening π interactions or to exploit this conformational duality to develop a partial agonist that finely modulates IL-18R signaling. A reduction in molecular weight by modifying non-essential peripheral groups would improve its pharmacokinetic profile (Ding and Xue 2024).

CNP0196376.4 represents a potential allosteric modulator. Despite a modest binding score (-9.80 kcal/mol) and two unfavorable interactions with SER24/THR29 attributable to steric or electrostatic repulsions, this ligand forms the largest number of hydrogen bonds in the MD simulation. Its high RMSD, prolonged adaptation phase, and gradual stabilization after 210 ns suggest an allosteric modulator mechanism rather than a classic competitive inhibitor (Jakubik and El-Fakahany 2020). The convergence of Rg (~ 2.30 nm) after 200 ns indicates that a state of equilibrium is reached, albeit with less favorable energy.

PCA reveals four phases with extensive conformational exploration and remarkable convergence between 150 and 250 ns, suggesting an induced fit mechanism where the ligand creates its own optimal binding pocket (Changeux & Edelstein, 2011). However, its frustrated FEL, with five to six shallow basins (5–15 kJ/mol) without a defined global minimum, is a warning sign. The regions of high induced flexibility (residues 200–220 and 270–320) could represent allosteric regulatory sites allowing fine modulation of IL-18R signaling. Its development requires kinetic binding studies, extended MD simulations (> 500 ns), and rational structure-activity analyses (Bernetti et al. 2017; Ding and Xue 2024).

Conclusion

These results highlight major mechanistic differences between the three ligands. CNP0188167.1 stands out as the priority candidate, combining the best binding affinity, exceptional conformational stability in MD, and a well-defined competitive inhibitory mechanism targeting THR29 in the active site of IL-18Rα. CNP0075206.3 is a promising secondary candidate that requires structural optimization to improve its stability. CNP0196376.4, although less effective by conventional criteria, represents an alternative therapeutic avenue via a potentially unique allosteric mechanism. This computational approach provides a rational basis for screening natural compounds and accelerates the development of new therapies for GVHD before experimental validation.

Limitations

This study is purely computational, and the absence of experimental validation (in vitro or in vivo) together with the complexity of the GvHD biological context limit the direct translatability of these findings to clinical settings Also, our study was planned to run a 400 ns MD simulation, but due to technical issues on the HPC MARWAN server, the dynamics stopped at 340 ns, and we were unable to reach 400 ns.

Declarations

AI Contribution

AI was used to create Python scripts, ameliorate MD and docking simulation commands, and reformulate and correct orthographic errors.

Conflict of interest

The authors reported no potential conflict of interest.

Ethics declaration

Not applicable

Funding

The author(s) reported there is no funding associated with the work featured in this article.

Author Contribution

LA, HC, and SR conceived the idea and designed the objectives. LA and SR performed the computational study, LA wrote the paper, HC participated in the data analysis, and HC, FG, and MB performed the corrections of the manuscript.

Acknowledgements

The authors gratefully acknowledge the High-Performance Computing platform Marwan, operated by the National Center for Scientific and Technical Research (CNRST), Rabat, Morocco, for providing the computational resources used to perform the molecular dynamics simulations in this study.

Data Availability

All data generated or analysed during this study are included in this published article and its supplementary information files.

References

1. Adasme, M. F. et al. PLIP 2021: expanding the scope of the protein–ligand interaction profiler to DNA and RNA. *Nucleic Acids Res.* **49**, W530–W534. https://doi.org/10.1093/nar/gkab294 (2021).
2. Bernetti, M., Cavalli, A. & Mollica, L. Protein-ligand (un)binding kinetics as a new paradigm for drug discovery at the crossroad between experiments and modelling. *Medchemcomm* **8**, 534–550. https://doi.org/10.1039/c6md00581k (2017).
3. Bouyahya, A. et al. Anti-inflammatory and analgesic properties of Moroccan medicinal plants: Phytochemistry, in vitro and in vivo investigations, mechanism insights, clinical evidences and perspectives. *J. Pharm. Anal.* **12**, 35–57. https://doi.org/10.1016/j.jpha.2021.07.004 (2022).
4. Chakravorty, A. et al. Exploring the Limits of the Generalized CHARMM and AMBER Force Fields through Predictions of Hydration Free Energy of Small Molecules. *J. Chem. Inf. Model.* **64**, 4089–4101. https://doi.org/10.1021/acs.jcim.4c00126 (2024).
5. Chandrasekhar, V. et al. COCONUT 2.0: a comprehensive overhaul and curation of the collection of open natural products database. *Nucleic Acids Res.* **53**, D634–D643. https://doi.org/10.1093/nar/gkae1063 (2025).
6. Diarra, A., Agossa, K. & Youl, E. N. H. The Potential of Cochlospermum tinctorium, Flueggea virosa, and Waltheria indica Traditional Plants From Burkina Faso in Treating Periodontitis: A Systematic Review. Cureus. (2024). https://doi.org/10.7759/cureus.52471
7. Dinarello, C. A. Novel targets for interleukin 18 binding protein. *Ann. Rheum. Dis.* **60**, iii18–iii24. https://doi.org/10.1136/ard.60.90003.iii18 (2001).
8. Dinarello, C. A. IL-18: A TH1 -inducing, proinflammatory cytokine and new member of the IL-1 family. *J. Allergy Clin. Immunol.* **103**, 11–24. https://doi.org/10.1016/S0091-6749(99)70518-X (1999).
9. Ding, Y. & Xue, X. Medicinal Chemistry Strategies for the Modification of Bioactive Natural Products. *Molecules* **29**, 689. https://doi.org/10.3390/molecules29030689 (2024).
10. Fujimori, Y. et al. Increased Expression of Interleukin-18 Receptor on T Lymphocytes in Patients with Acute Graft-versus-Host Disease After Allogeneic Bone Marrow Transplantation. *J. Interferon Cytokine Res.* **22**, 751–754. https://doi.org/10.1089/107999002320271332 (2002).
11. Gohlke, H. & Klebe, G. Approaches to the Description and Prediction of the Binding Affinity of Small-Molecule Ligands to Macromolecular Receptors. *Angew Chem. Int. Ed.* **41**, 2644–2676. https://doi.org/10.1002/1521-3773(20020802)41 (2002). :15%253C2644::AID-ANIE2644%253E3.0.CO;2-O.
12. Goodsell, D. S., Sanner, M. F., Olson, A. J. & Forli, S. The AutoDock suite at 30. *Protein Sci.* **30**, 31–43. https://doi.org/10.1002/pro.3934 (2021).
13. Itoi, H. et al. Differential Upregulation of Interleukin-18 Receptor α Chain Between $CD4^+$ and $CD8^+$ T Cells During Acute Graft-Versus-Host Disease in Mice. *J. Interferon Cytokine Res.* **24**, 291–296. https://doi.org/10.1089/107999004323065075 (2004).
14. Jakubik, J. & El-Fakahany, E. E. Current Advances in Allosteric Modulation of Muscarinic Receptors. *Biomolecules* **10**, 325. https://doi.org/10.3390/biom10020325 (2020).
15. Kanate, A. S. et al. Indications for Hematopoietic Cell Transplantation and Immune Effector Cell Therapy: Guidelines from the American Society for Transplantation and Cellular Therapy. *Biol. Blood Marrow Transplant.* **26**, 1247–1256. https://doi.org/10.1016/j.bbmt.2020.03.002 (2020).
16. Kaplan, W. Swiss-PDB Viewer (Deep View). *Brief. Bioinform.* **2**, 195–197. https://doi.org/10.1093/bib/2.2.195 (2001).
17. Khalfaoui, A. et al. LC-ESI/MS-Phytochemical Profiling with Antioxidant, Antibacterial, Antifungal, Antiviral and In Silico Pharmacological Properties of Algerian Asphodelus tenuifolius. *(Cav) Org. Extracts Antioxid.* **10**, 628.

https://doi.org/10.3390/antiox10040628 (2021).

18. Li, X. et al. Protective effect of neutralizing anti-IL-18α monoclonal antibody on a mouse model of acute graft-versus-host disease. *Oncol. Rep.* **34**, 2031–2039. https://doi.org/10.3892/or.2015.4176 (2015).
19. Malard, F. et al. Acute graft-versus-host disease. *Nat. Rev. Dis. Primers*. **9**, 27. https://doi.org/10.1038/s41572-023-00438-1 (2023).
20. Morris, G. M. et al. AutoDock4 and AutoDockTools4: Automated docking with selective receptor flexibility. *J. Comput. Chem.* **30**, 2785–2791. https://doi.org/10.1002/jcc.21256 (2009).
21. Nakamura, K. et al. Endotoxin-induced serum factor that stimulates gamma interferon production. *Infect. Immun.* **57**, 590–595. https://doi.org/10.1128/iai.57.2.590-595.1989 (1989).
22. Nakmode, D. D. et al. Long-acting parenteral formulations of hydrophilic drugs, proteins, and peptide therapeutics: mechanisms, challenges, and therapeutic benefits with a focus on technologies. *Drug Deliv Transl Res.* **15**, 1156–1180. https://doi.org/10.1007/s13346-024-01747-y (2025).
23. Pusic, I. & Pavletic, S. Z. Challenges in Conducting Studies in Chronic Graft-versus-Host Disease. CHI 1:36. (2019). https://doi.org/10.2991/chi.d.190314.001
24. Qiang, Y. et al. Structural basis of the multiple ligand binding mechanisms of the P2X1 receptor. *Acta Pharmacol. Sin*. **46**, 2564–2573. https://doi.org/10.1038/s41401-025-01512-y (2025).
25. Reddy, P. et al. In response to American Society of Hematology 2020 guidelines for treating newly diagnosed acute myeloid leukemia in older adults. *Blood Adv.* **4**, 5431–5432. https://doi.org/10.1182/bloodadvances.2020003413 (2020).
26. Reichenbach, D. K. et al. The IL-33/ST2 axis augments effector T-cell responses during acute GVHD. *Blood* **125**, 3183–3192. https://doi.org/10.1182/blood-2014-10-606830 (2015).
27. Rex, D. A. B. et al. A comprehensive pathway map of IL-18-mediated signalling. *J. Cell. Commun. Signal.* **14**, 257–266. https://doi.org/10.1007/s12079-019-00544-4 (2020).
28. Sorokina, M. et al. COCONUT online: Collection of Open Natural Products database. *J. Cheminform*. **13**, 2. https://doi.org/10.1186/s13321-020-00478-9 (2021).
29. Talley, S., Rademacher, D. J. & Campbell, E. M. Inflammasome activation occurs in CD4 + and CD8 + T cells during graft-versus-host disease. *Cell. Death Dis.* **14**, 632. https://doi.org/10.1038/s41419-023-06138-8 (2023).
30. Teshima, T., Reddy, P. & Zeiser, R. Acute Graft-versus-Host Disease: Novel Biological Insights. *Biol. Blood Marrow Transplant.* **22**, 11–16. https://doi.org/10.1016/j.bbmt.2015.10.001 (2016).
31. Trott, O. & Olson, A. J. AutoDock Vina: Improving the speed and accuracy of docking with a new scoring function, efficient optimization, and multithreading. *J. Comput. Chem.* **31**, 455–461. https://doi.org/10.1002/jcc.21334 (2010).
32. Tsutsumi, N. et al. The structural basis for receptor recognition of human interleukin-18. *Nat. Commun.* **5**, 5340. https://doi.org/10.1038/ncomms6340 (2014).
33. Walters, W. P. Going further than Lipinski's rule in drug design. *Expert Opin. Drug Discov.* **7**, 99–107. https://doi.org/10.1517/17460441.2012.648612 (2012).
34. Xu, X. et al. Anti-inflammatory activity of injectable dexamethasone acetate-loaded nanostructured lipid carriers. *Drug Deliv.* **18**, 485–492. https://doi.org/10.3109/10717544.2011.589087 (2011).
35. Zhang, L., Chu, J., Yu, J. & Wei, W. Cellular and molecular mechanisms in graft-versus-host disease. *J. Leukoc. Biol.* **99**, 279–287. https://doi.org/10.1189/jlb.4RU0615-254RR (2016).

Figures

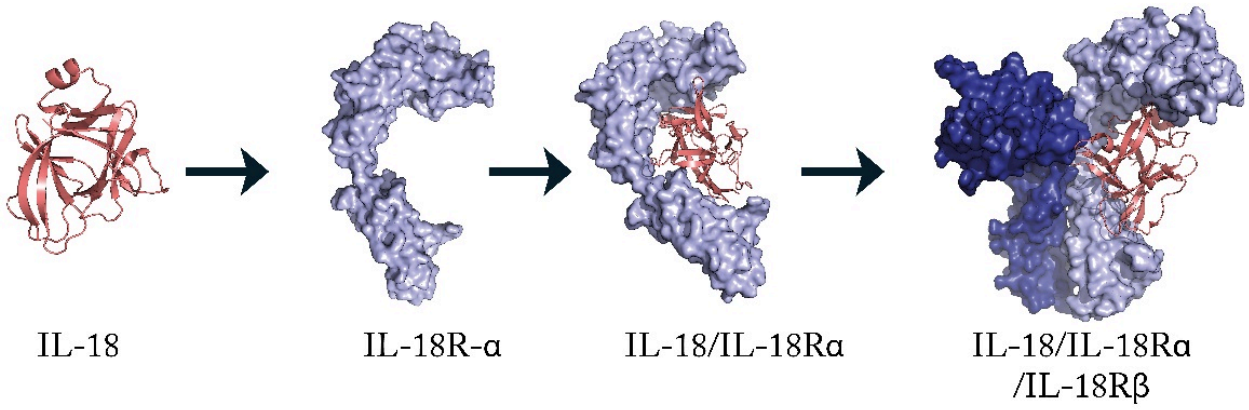


Figure 1

Structural assembly of IL-18/IL-18 receptor complex

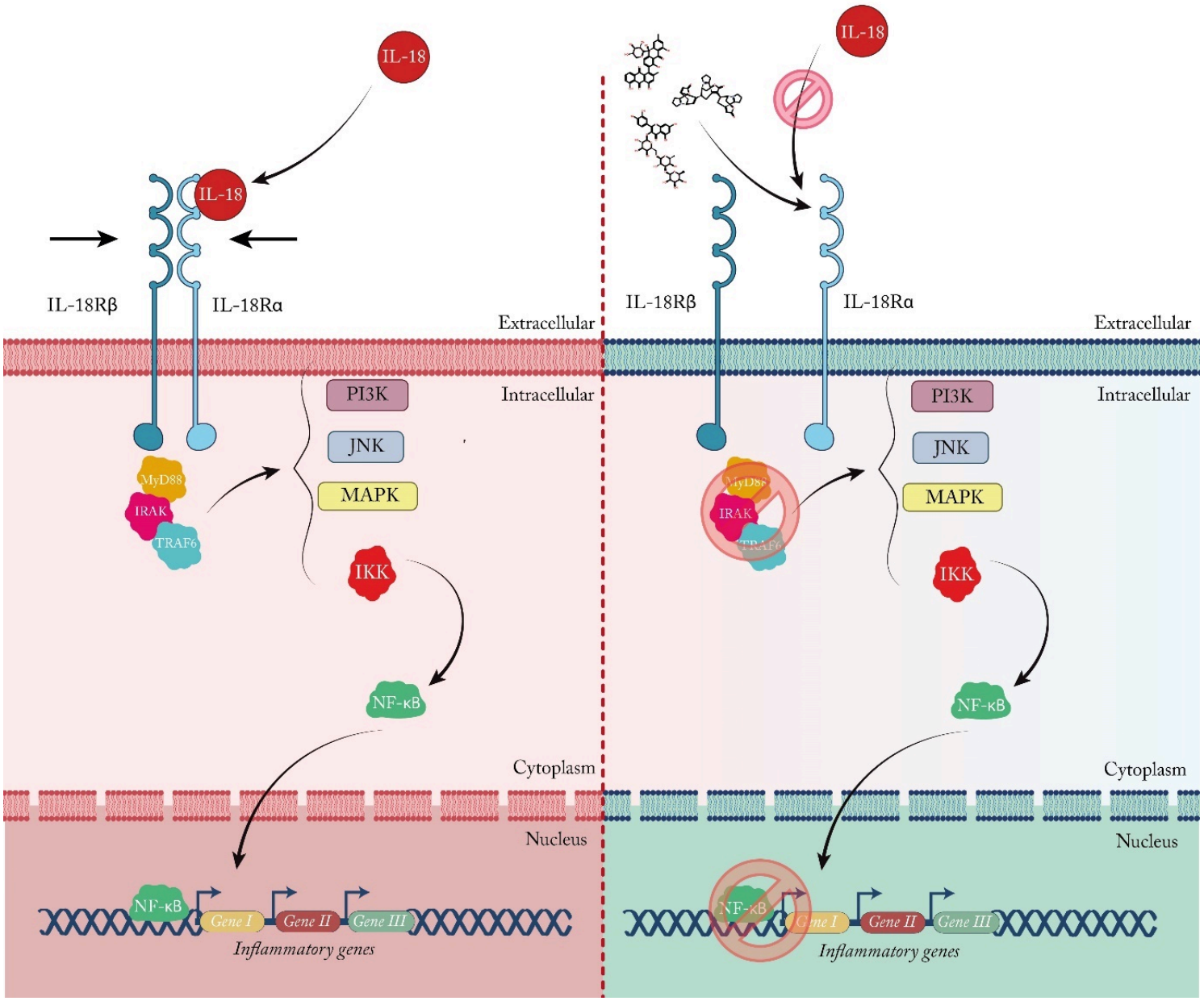


Figure 2

Schematic representation of the IL-18/IL-18R signaling pathway. In red indicate the canonical signaling cascade under normal physiological conditions; In blue denote pathway components targeted and inhibited by natural compound inhibitors.

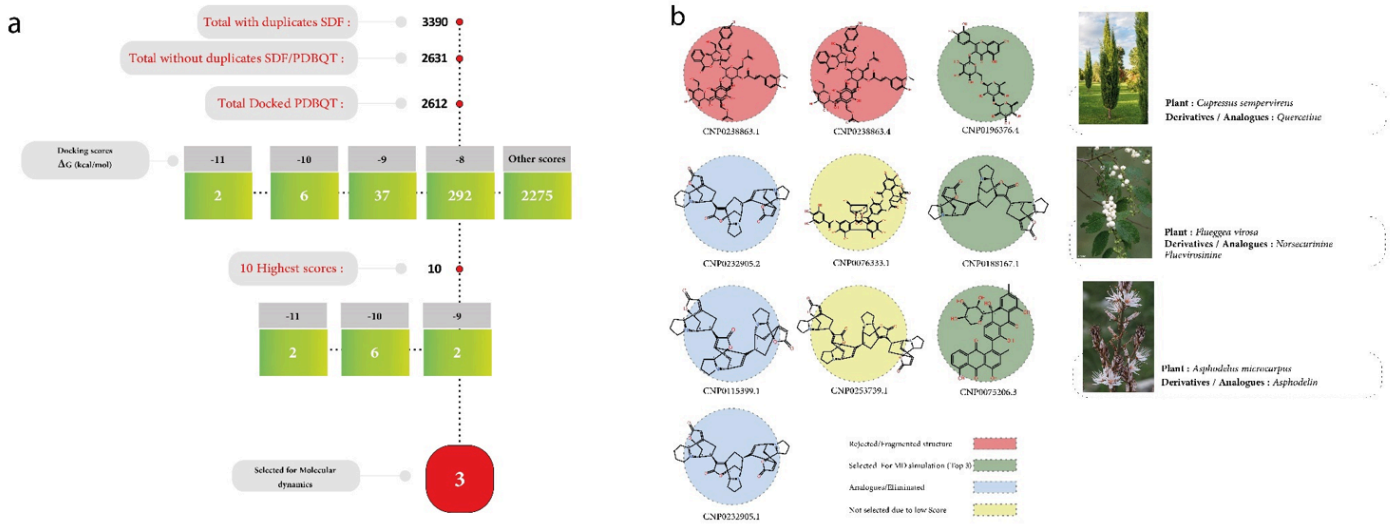


Figure 3

a) Virtual screening workflow and compound selection for molecular dynamics simulations.

b) Chemical structures and plant sources of selected natural compounds and their structural analogs. Among the 10 molecules with the highest binding affinities, three were selected for molecular dynamics simulation after elimination of fragmented structures (red), redundant analogues (blue), and compounds with low Selection scores (yellow). The three molecules selected (green) come from different Moroccan medicinal plants: **CNP0188167.1**, a securinane-type alkaloid (analog of Norsecurinine/Fluevirosinine) isolated from Flueggea virosa; **CNP0075206.3**, an anthraquinone dimer known as Asphodeline from Asphodelus microcarpus; and **CNP0196376.4**, a flavonoid derived from quercetin extracted from Cupressus sempervirens.

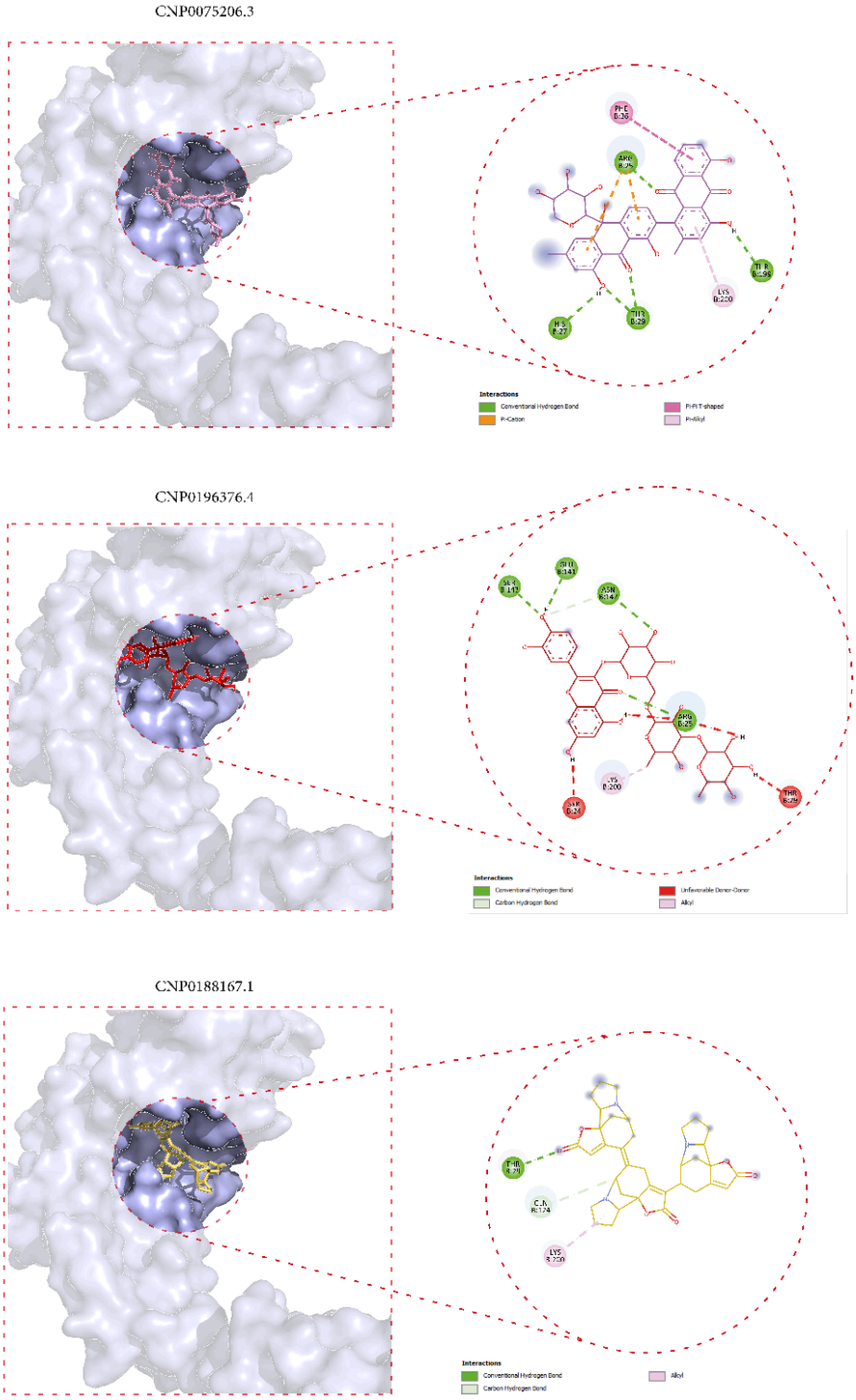


Figure 4

Discovery Studio analysis of the three best IL-18R ligands

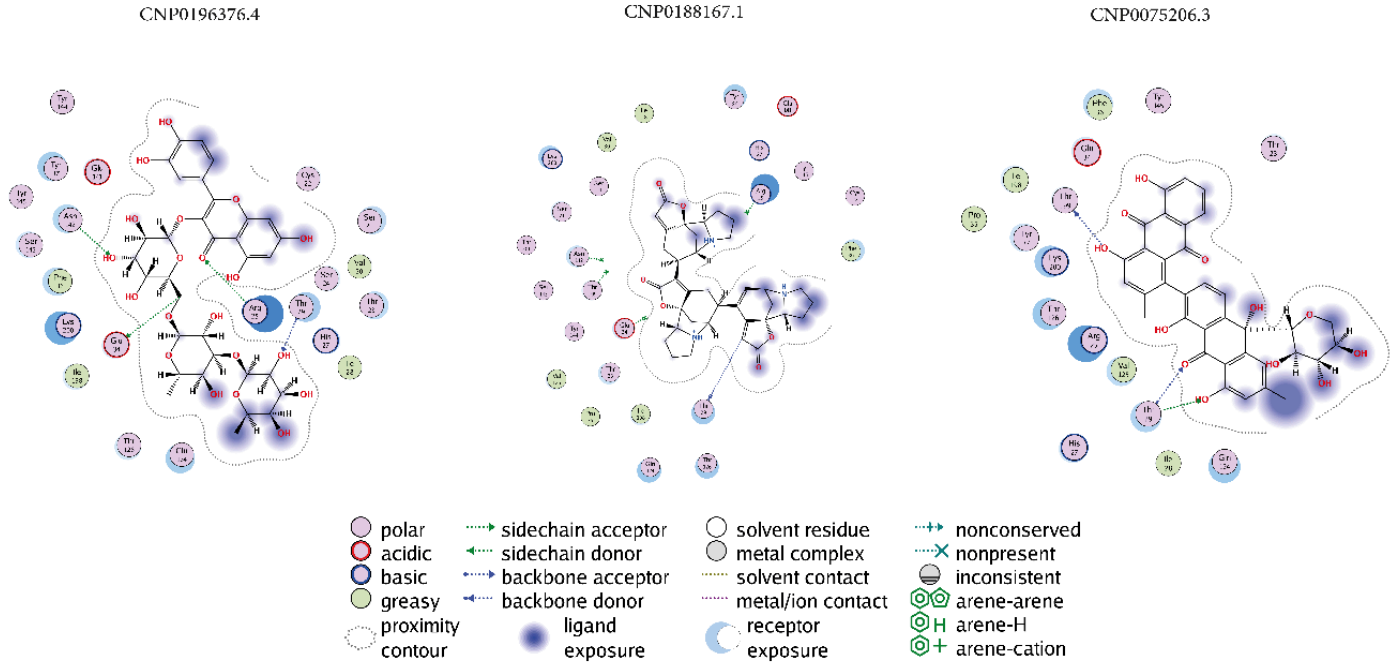


Figure 5

MOE analysis of the three best IL-18R ligands

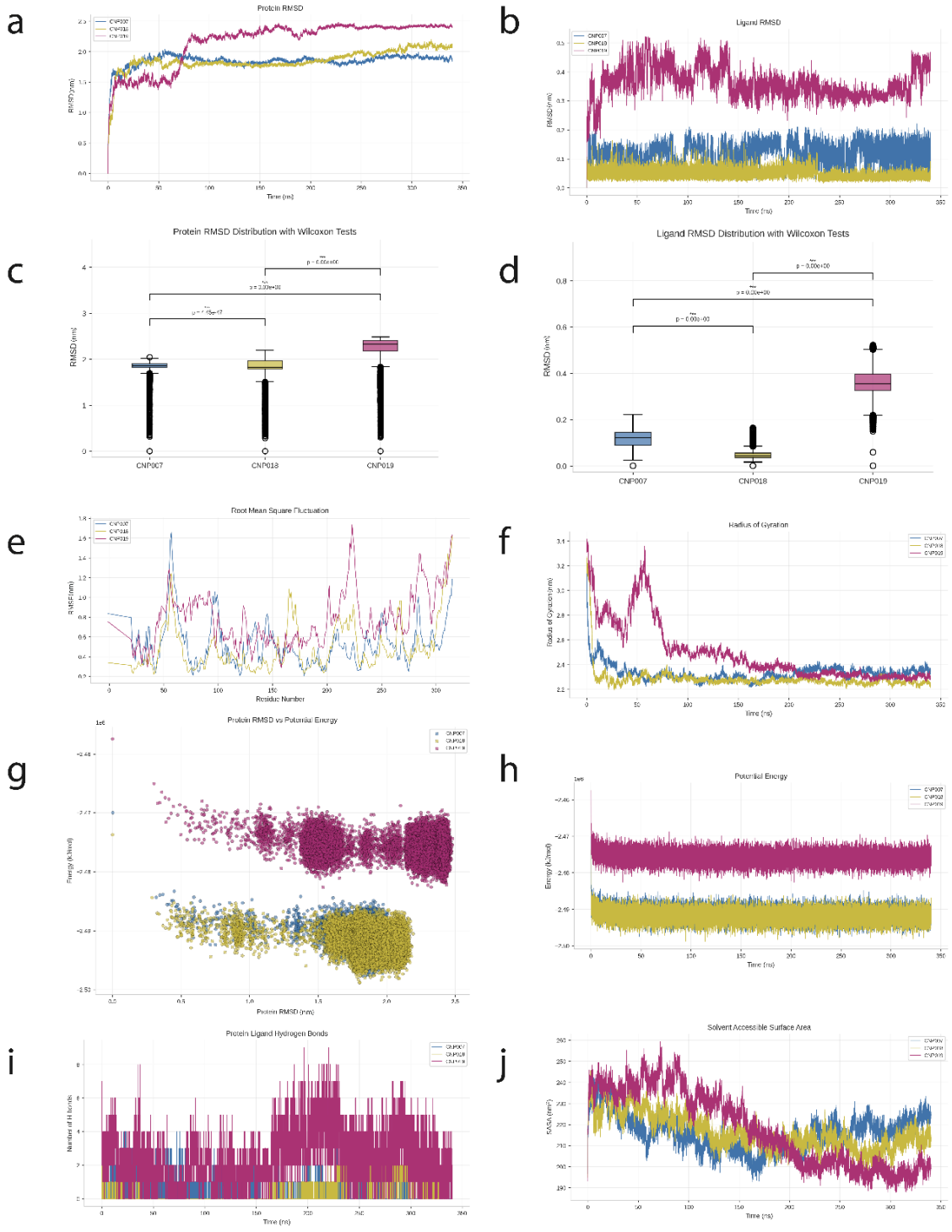


Figure 6

Principal Molecular Dynamics analysis of the complexes (Protein-ligands), **a)**Evolution of the root mean square deviation (RMSD) of the Cα atoms of the protein, B) RMSD Profile of the ligand only, **c-d)** Boxplots represent the Distribution of **c)** Protein RMSD and **d)** Ligand values. The significance of the differences observed between the complexes was evaluated by the Wilcoxon test (*p < 0,05),* **e)** Root mean square fluctuations (RMSF) of the protein residues, **f)** Radius of gyration (Rg) Profile of the complexes, **g)** Dispersion Graphic, Correlating Protein RMSD values with potential energy, **h)** Potential energy profile during the simulation for each complex, **i)** Number of hydrogen bonds

(HBonds) between the protein-ligand complex au during the simulation, **j)** Evolution of Surface accessible solvent analysis (SASA), measuring the exposure changes of the residues to the solvent.

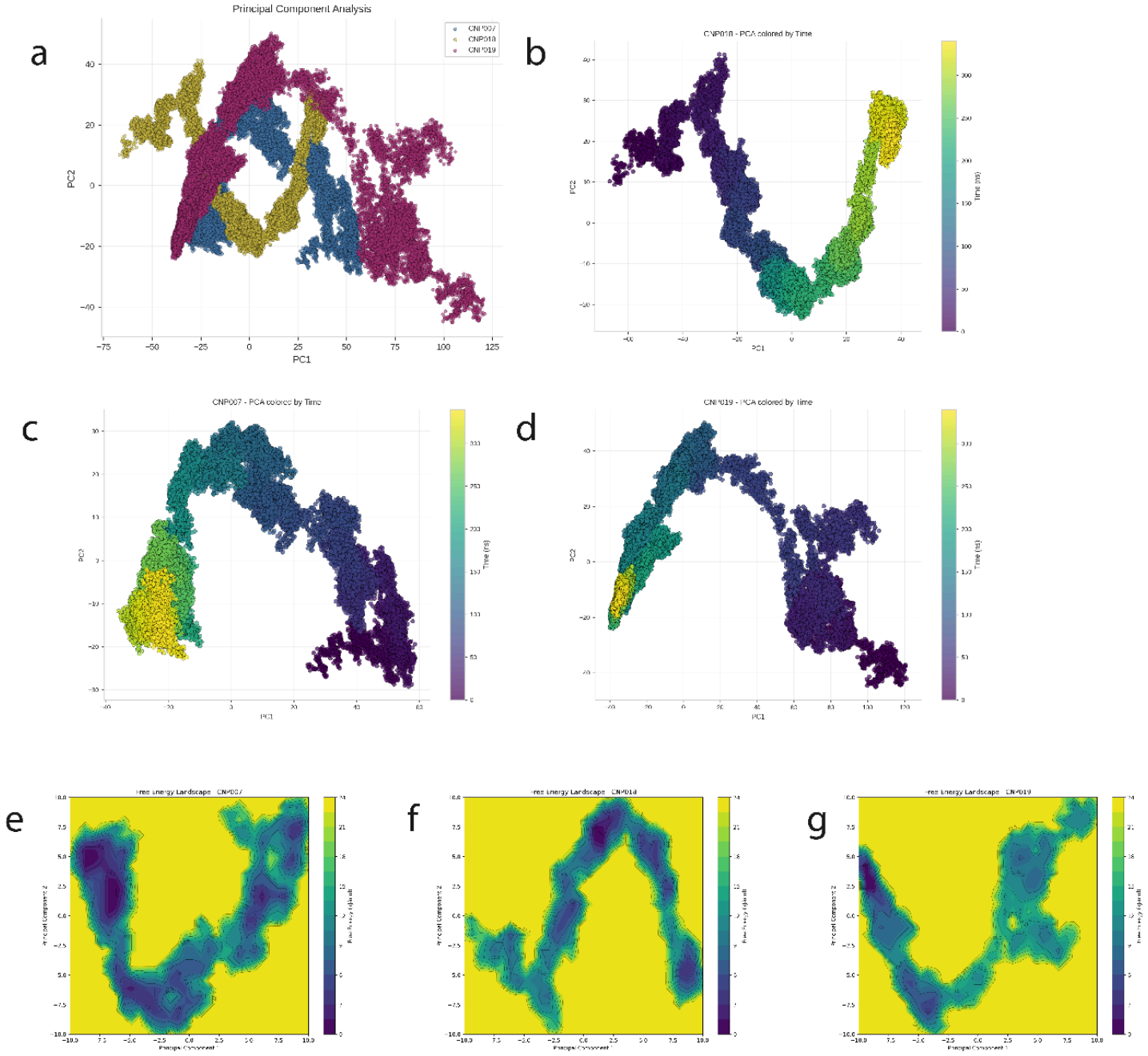


Figure 7

Secondary Molecular Dynamics analysis of the complexes (Protein-ligands), **a)** Principal component analysis (PCA) evaluates the relevant preferential conformations explored by the system, **b-c-d)** Temporal evolution of the PCA illustrates the major conformations during the simulation, **e-f-g)** Free energy landscape (FEL), constructed using PC1-PC2 analysis, free energy values are expressed by kJ/mol^{-1}.

Supplementary Files

This is a list of supplementary files associated with this preprint. Click to download.

- MDresult.sh
- MDprep.sh
- MDsimul.sh
- READMEPythonscripts.txt
- VinaDocking.sh
- PlotsPCATIMEBOXPLOTSRMSDVSENERGY.py
- ObableConversion.sh
- PlotsRMSDRMSFRGHBONDSSASAENERGY.py
- PlotsFEL.py
- DockingResultsSUPDATA.xlsx